Bulgarian Journal of Physics vol. **46** (2019) 247–258

Multiple Quantum Phase Transitions in the Zr Isotopes

N. Gavrielov[1], **A. Leviatan**[1], **F. Iachello**[2]
[1]Racah Institute of Physics, The Hebrew University, Jerusalem 91904, Israel
[2]Center for Theoretical Physics, Sloane Physics Laboratory, Yale University, New Haven, Connecticut 06520-8120, USA

Received *10 November 2019*

Abstract. We present a detailed analysis of spectra and other observables for the entire chain of Zr isotopes, from neutron number 52 to 70, in the framework of the interacting boson model with configuration mixing. The results suggest a remarkable interplay of multiple quantum phase transitions (QPTs). One type of QPT involves an abrupt crossing of normal and intruder configurations, superimposed on a second type of QPT involving gradual shape-changes within each configuration.

KEY WORDS: Quantum shape-phase transitions, configuration-crossing, interacting boson model with configuration mixing, Zr isotopes.

1 Introduction

Quantum phase transitions (QPTs) are qualitative changes in the structure of a physical system induced by a change in one or more parameters that appear in the quantum Hamiltonian describing the system. Such ground-state phase transitions [1,2] have been the subject of many investigations in nuclear physics [3–5], where most of the attention has been devoted to shape phase transitions in a single configuration, described by a single Hamiltonian of the form,

$$\hat{H} = (1-\xi)\,\hat{H}_1 + \xi \hat{H}_2\ . \tag{1}$$

As the control parameter ξ changes from 0 to 1, the symmetry and equilibrium shape of the system change from those of $\hat{H}_1$ to those of $\hat{H}_2$. For sake of clarity, we denote these phase transitions Type I. The latter have been observed in the neutron number 90 region, *e.g.*, for Nd-Sm-Gd isotopes [4].

A different type of phase transitions occurs when two (or more) configurations coexist [6]. In this case, the quantum Hamiltonian has a matrix form [7]

$$\hat{H} \;=\; \begin{bmatrix} \hat{H}_A(\xi_A) & \hat{W}(\omega) \\ \hat{W}(\omega) & \hat{H}_B(\xi_B) \end{bmatrix}\ , \tag{2}$$

where the index A, B denotes the two configurations and $\hat{W}$ denotes their coupling. We call for sake of clarity these phase transitions Type II, to distinguish them from those of a single configuration. The latter have been observed in nuclei near shell closure, *e.g.*, in the light Pb-Hg isotopes [6].

As the control parameters (ξ_A, ξ_B, ω) in Eq. (2) are varied, the separate Hamiltonians $\hat{H}_A$ and $\hat{H}_B$ can undergo shape-phase transitions of Type I, and the combined Hamiltonian can experience a Type-II crossing of configurations A and B. In most cases encountered in nuclei, the separate QPTs are masked by the strong mixing between the two configurations. In the present contribution, we show that the Zr isotopes are exceptional in the sense that the crossing is abrupt, the separate configurations retain their purity before and after the crossing, and the shape evolution of each configuration can be cast in terms of its own phase transition. This results in an intricate interplay of intertwined multiple QPTs [8].

2 The IBM with Configuration Mixing in the Zr Chain

The $_{40}$Zr isotopes have been recently the subject of several experimental investigations [9–15] and theoretical studies, including mean-field based methods [16–18], the Monte-Carlo shell-model (MCSM) [19] and algebraic methods [8,20]. We adapt here the algebraic approach of the Interacting Boson Model (IBM) [21], with bosons representing valence nucleon pairs counted from the nearest closed shells. This provides a simple tractable framework, where phases of quadrupole shapes: spherical, prolate-deformed and γ-unstable deformed, correspond to U(5), SU(3) and SO(6) dynamical symmetries, respectively.

To be specific, we use the configuration mixing model (IBM-CM) of [22], and write the Hamiltonian not in matrix form, but rather in the equivalent form $\hat{H} = \hat{H}_A^{(N)} + \hat{H}_B^{(N+2)} + \hat{W}^{(N,N+2)}$, where $\hat{\mathcal{O}}^{(N)} = \hat{P}_N^\dagger \hat{\mathcal{O}} \hat{P}_N$ and $\hat{\mathcal{O}}^{(N,N')} = \hat{P}_N^\dagger \hat{\mathcal{O}} \hat{P}_{N'}$, for an operator $\hat{\mathcal{O}}$, with $\hat{P}_N$, a projection operator onto the $[N]$ boson space. Here $\hat{H}_A^{(N)}$ represents the so-called normal (N boson space) configuration and $\hat{H}_B^{(N+2)}$ represents the so-called intruder ($N+2$ boson space) configuration. Similar to a calculation done for the $_{42}$Mo isotopes in [23], we consider $^{90}_{40}$Zr$_{50}$ as a core and valence neutrons in the 50-82 major shell. The normal A-configuration corresponds to having no active protons above the $Z = 40$ subshell gap, and the intruder B-configuration corresponds to two-proton excitation from below to above this gap, creating 2p-2h states (see Figure 1 of [23]). The explicit form of the Hamiltonians employed in the current study is

$$\hat{H}_A = \epsilon_d^{(A)} \hat{n}_d + \kappa^{(A)} \hat{Q}_\chi \cdot \hat{Q}_\chi \,, \tag{3a}$$

$$\hat{H}_B = \epsilon_d^{(B)} \hat{n}_d + \kappa^{(B)} \hat{Q}_\chi \cdot \hat{Q}_\chi + \kappa'^{(B)} \hat{L} \cdot \hat{L} + \Delta_p \,, \tag{3b}$$

$$\hat{W} = \omega \left[(d^\dagger \times d^\dagger)^{(0)} + (s^\dagger)^2 \right] + \text{H.c.} \,, \tag{3c}$$

where H.c. stands for Hermitian conjugate. The quadrupole operator is defined

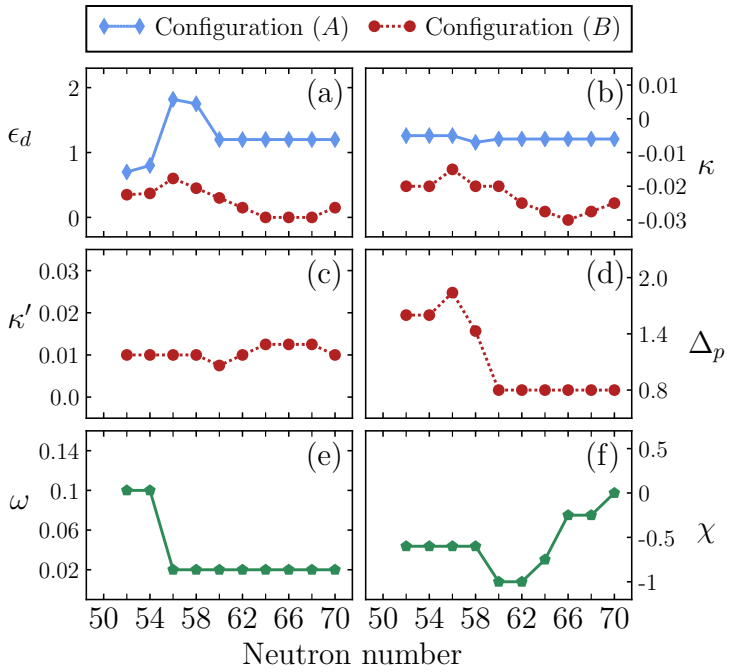

Figure 1. Parameters of the IBM-CM Hamiltonian, Eq. (3), are in MeV, except for the parameter χ which is dimensionless. Based on Table I of [8].

as $\hat{Q}_\chi = d^\dagger s + s^\dagger \tilde{d} + \chi(d^\dagger \times \tilde{d})^{(2)}$ and $\hat{n}_d$ is the d-boson number operator. In Eq. (3b), Δ_p is the off-set between the normal and intruder configurations, where the index p denotes the fact that this is a proton excitation. Such Hamiltonians have been used extensively for studying coexistence phenomena nuclei [22–26]. The resulting eigenstates $|\Psi; L\rangle$ with angular momentum L, are linear combinations of the wave functions, Ψ_A and Ψ_B, in the two spaces $[N]$ and $[N+2]$,

$$|\Psi; L\rangle = a\ |\Psi_A; [N], L\rangle + b\ |\Psi_B; [N+2], L\rangle\ , \tag{4}$$

with $a^2 + b^2 = 1$.

By employing the IBM-CM framework described above, we have calculated the spectra and other observables of the entire chain of Zr isotopes, from neutron number 52 to 70. The values of the Hamiltonian parameters, obtained by a global fit to energy and $E2$ data, are shown in Figure 1, and are consistent with those of previous calculations in this mass region [23]. It should be noted that beyond the middle of the shell, at neutron number 66, bosons are replaced by boson holes [21]. Apart from some fluctuations due to the subshell closure at neutron number 56 (the filling of the $2d_{5/2}$ orbital), the values of the parameters are a smooth function of neutron number and, in some cases, a constant. A

notable exception is the sharp decrease by 1 MeV of the energy off-set parameter Δ_p beyond neutron number 56. Such a behavior was observed for the Mo and Ge chains and, as noted in [23], it reflects the effects of the isoscalar residual interaction between protons and neutrons occupying the partner orbitals $1g_{9/2}$ and $1g_{7/2}$, which is the established mechanism for descending cross shell-gap excitations and onset of deformation in this region [27–29]. The $E2$ operator reads $\hat{T}(E2) = e^{(A)}\hat{Q}_\chi^{(N)} + e^{(B)}\hat{Q}_\chi^{(N+2)}$, where $\hat{Q}_\chi^{(N)} = \hat{P}_N^\dagger \hat{Q}_\chi \hat{P}_N$, $\hat{Q}_\chi^{(N+2)} = P_{N+2}^\dagger \hat{Q}_\chi \hat{P}_{N+2}$ and $\hat{Q}_\chi$ is the same operator as in the Hamiltonian (3). The boson effective charges are $e^{(A)} = 0.9$ and $e^{(B)} = 2.24$ $(\mathrm{W.u.})^{1/2}$.

3 Evolution of Spectra along the Zr Chain

An important clue for understanding the change in structure of the Zr isotopes, is obtained by examining the evolution of their spectra along the chain. In Figure 2, we show a comparison between experimental and calculated levels, together with assignments to configurations based on Eq. (4), and to the closest

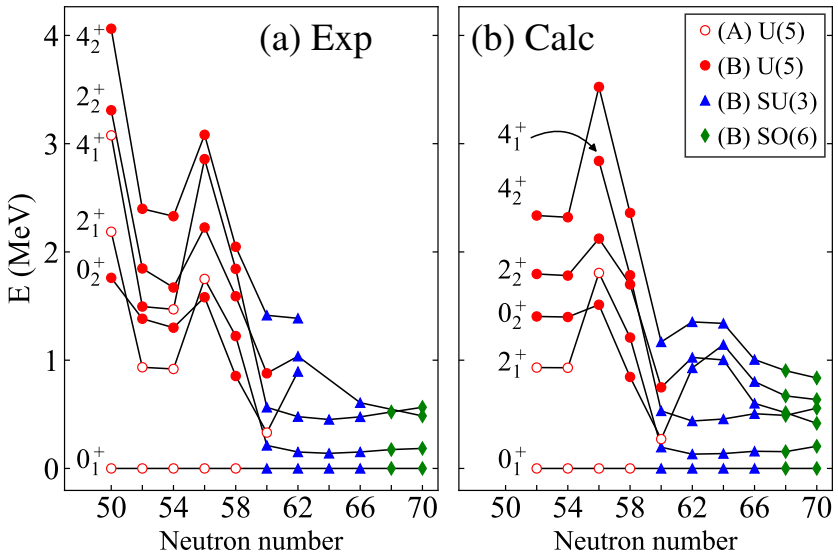

Figure 2. Comparison between (a) experimental [13, 31] and (b) calculated energy levels $0_1^+, 2_1^+, 4_1^+, 0_2^+, 2_2^+, 4_2^+$. Empty (filled) symbols indicate a state dominated by the normal A-configuration (intruder B-configuration), with assignments based on the decomposition of Eq. (4). The shape of the symbol [$\circ$, $\triangle$, $\Diamond$], indicates the closest dynamical symmetry [U(5), SU(3), SO(6)] to the level considered. Note that the calculated values start at neutron number 52, while the experimental values include the closed shell at 50. Adapted from [8].

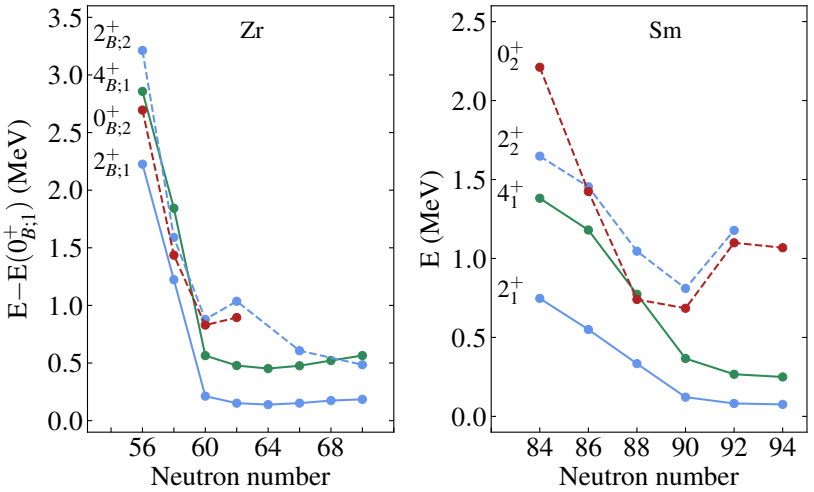

Figure 3. Left panel: Experimental excitation energies for states of the intruder B-configuration (denoted by $L^+_{B;i}$) in the $_{40}$Zr isotopes, with respect to the lowest state ($0^+_{B;1}$) of that configuration. Right panel: Typical features of a U(5)-SU(3) Type I QPT manifested in the empirical spectra of the $_{62}$Sm isotopes. Data taken from [31].

dynamical symmetry for each level. One can see here a rather complex structure. In the region between neutron number 50 and 56, there appear to be two configurations, one spherical (seniority-like), (A), and one weakly deformed, (B), as evidenced by the ratio $R_{4/2}$ in each configuration which is at 52-56, $R^{(A)}_{4/2} \cong 1.6$ and $R^{(B)}_{4/2} \cong 2.3$. From neutron number 58, there is a pronounced drop in energy for the states of configuration (B), and at 60, the two configurations exchange their roles, indicating a Type II QPT. At this stage, the intruder configuration (B) appears to be at the critical point of a U(5)-SU(3) Type I QPT, as evidenced by the low value of the excitation energy of the first-excited 0^+ state of the B configuration, (denoted by $0^+_{B;2}$ in the left panel of Figure 3). The same situation occurs in the $_{62}$Sm and $_{64}$Gd isotopes at neutron number 90 [21,30], as is clearly shown in Figure 3. Beyond neutron number 60, the intruder configuration (B) becomes progressively strongly deformed, as evidenced by the small value of the excitation energy of the state 2^+_1, $E_{2^+_1} = 151.78$ keV and by the ratio $R^{(B)}_{4/2} = 3.15$ in ^{102}Zr, and $E_{2^+_1} = 139.3$ keV, $R^{(B)}_{4/2} = 3.24$ in ^{104}Zr. At still larger neutron number 66, the ground state band becomes γ-unstable, as evidenced by the close energy of the states 2^+_2 and 4^+_1, $E_{2^+_2} = 607.0$ keV, $E_{4^+_1} = 476.5$ keV, in ^{106}Zr, and especially by the recent results $E_{4^+_1} = 565$ keV and $E_{2^+_2} = 485$ keV in ^{110}Zr [13], a signature of the SO(6) symmetry. In this region, the ground state configuration undergoes a crossover from SU(3) to SO(6).

4 Type I and Type II QPTs in the Zr Chain

The above spectral analysis signal the presence of multiple QPTs in the Zr isotopes. In order to understand the nature of these phase transitions, it is instructive to examine in more detail the way in which the structure of the states evolves, and the behaviour of the order parameters.

Information on configuration-changes can be inferred from the probabilities a^2 or b^2, Eq. (4), of the states considered. Figure 4 shows the percentage of the wave function within the intruder configuration for the ground state (0_1^+) and first-excited state (2_1^+) as a function of neutron number along the Zr chain. The rapid change in structure of the 0_1^+ state from the normal A-configuration ($b^2=1.8\%$) in ^{98}Zr to the intruder B-configuration ($b^2=87.2\%$) in ^{100}Zr, is clearly evident. The jump in configurations appears sooner in the 2_1^+ state, which changes to configuration B ($b^2=97.1\%$) already in ^{98}Zr, as pointed out in [14]. Outside a narrow region near neutron number 60 where the crossing occurs, the two configurations are weakly mixed and the states retain a high level of purity (*i.e.*, $b^2\approx 0\%$ or 100%).

Information on shape-changes can be obtained by examining the relevant order parameters of the phase transitions. In the present study, the latter involve the expectation value of $\hat{n}_d$ in the ground state wave function, $|\Psi; L=0_1^+\rangle$ and in its Ψ_A and Ψ_B components (4), denoted by $\langle\hat{n}_d\rangle_{0_1^+}$, $\langle\hat{n}_d\rangle_A$, and $\langle\hat{n}_d\rangle_B$. Here $\langle\hat{n}_d\rangle_A$ and $\langle\hat{n}_d\rangle_B$ portray the shape of configuration (A) and (B), respectively, and $\langle\hat{n}_d\rangle_{0_1^+}=a^2\langle\hat{n}_d\rangle_A+b^2\langle\hat{n}_d\rangle_B$ portrays also the dependence on the normal-intruder mixing. Figure 5 shows the evolution along the Zr chain of these order parameters ($\langle\hat{n}_d\rangle_A$, $\langle\hat{n}_d\rangle_B$ in dotted and $\langle\hat{n}_d\rangle_{0_1^+}$ in solid lines), normalized by the respective boson numbers. Configuration (A) is seen to be spherical for all neutron numbers considered. In contrast, configuration (B) is weakly-deformed for neutron number 52-58. One can see here clearly the imprints of the jump,

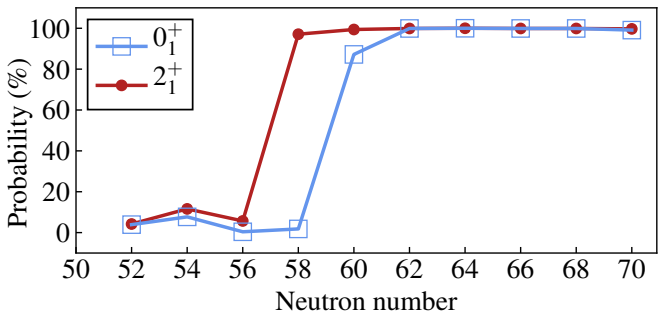

Figure 4. Percentage of the wave functions within the intruder B-configuration [the b^2 probability in Eq. (4)], for the ground (0_1^+) and excited (2_1^+) states in each Zr isotope.

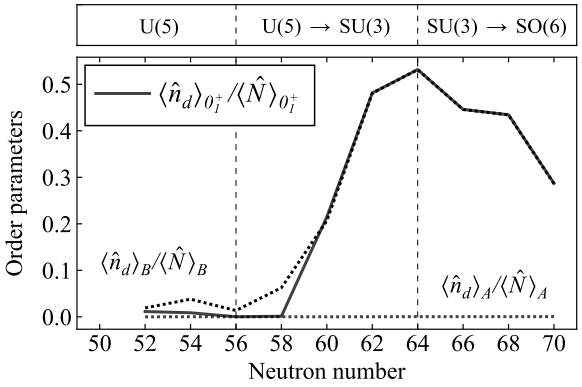

Figure 5. Evolution of order parameters along the Zr chain. The latter are the calculated expectation values of $\hat{n}_d$ in the total ground state wave function $|\Psi; L = 0_1^+\rangle$, Eq. (4) (solid line) and in its (A) and (B) components (dotted lines), normalized by the respective boson numbers $\langle \hat{N} \rangle_{0_1^+} = a^2 N + b^2(N+2)$, $\langle \hat{N} \rangle_A = N$, $\langle \hat{N} \rangle_B = N+2$. Adapted from [8].

noted in Figure 4 between neutron number 58 and 60, from configuration (A) to configuration (B), indicating a first-order Type II QPT, a further increase at neutron numbers 60-64 indicating a U(5)-SU(3) Type I QPT within configuration (B), and, finally, there is a decrease at neutron number 66, due in part to the crossover from SU(3) to SO(6) and in part to the shift from boson particles to boson holes after the middle of the major shell 50-82. $\langle \hat{n}_d \rangle_{0_1^+}$ is close to $\langle \hat{n}_d \rangle_A$ for neutron number 52-58 and coincides with $\langle \hat{n}_d \rangle_B$ at 60 and above, consistent with a high degree of purity with respect to configuration-mixing.

The combined analyses of energy spectra (Figure 2), wave-functions (Figure 4) and order parameters (Figure 5), suggests a remarkable interplay of configurations-interchange and shape-evolution in the Zr isotopes, manifesting simultaneously multiple QPTs with different character. Specifically, a Type II QPT involves an abrupt crossing of the normal and intruder configurations. This local effect is superimposed on a Type I QPT which involves a gradual shape-change within each configuration. In particular, the normal A-configuration remains spherical along the Zr chain, while the intruder B-configuration undergoes a first-order U(5) $\rightarrow$ SU(3) (spherical to prolate-deformed) transition and an SU(3) $\rightarrow$ SO(6) (prolate to γ-unstable deformed) crossover.

5 Empirical Signatures

Further evidence for the scenario of multiple QPTs in the Zr isotopes, is obtained by an analysis of other observables, such as $E2$ transition rates, isotope shifts and two-neutron separation energies.

As shown in Figure 6(a), the calculated $B(E2)$'s agree with the empirical values and follow the same trends as the respective order parameters. The dotted lines denote calculated $E2$ transitions between states within the same configuration. The calculated $2^+_A \rightarrow 0^+_A$ transition rates coincide with the empirical $2^+_1 \rightarrow 0^+_1$ rates for neutron number 52-56. The calculated $2^+_B \rightarrow 0^+_B$ transition rates coincide with the empirical $2^+_2 \rightarrow 0^+_2$ rates for neutron number 52-56, with the empirical $2^+_1 \rightarrow 0^+_2$ rates at neutron number 58, and with the empirical $2^+_1 \rightarrow 0^+_1$ rates at neutron number 60-64. The large jump in $B(E2; 2^+_1 \rightarrow 0^+_1)$ between neutron number 58 and 60 reflects the passing through a critical point, common to a Type II QPT involving a crossing of two configurations and a spherical to deformed Type I QPT within the B configuration. The further increase in $B(E2; 2^+_1 \rightarrow 0^+_1)$ for neutron numbers 60-64 is as expected for such a U(5)-SU(3) QPT (see Figure 2.20 in [21]) and, as seen in Figure 5, it reflects an increase of the deformation in a spherical to deformed shape-phase transition. The subsequent decrease from the peak at neutron number 64 towards 70, is in accord with an SU(3) to SO(6) crossover (see Figure 2.22 in [21]).

Further evidence for the indicated structural changes occurring in the Zr chain, can be obtained from an analysis of the isotope shift $\Delta \langle \hat{r}^2 \rangle_{0^+_1} = \langle \hat{r}^2 \rangle_{0^+_1;A+2} - \langle \hat{r}^2 \rangle_{0^+_1;A}$, where $\langle \hat{r}^2 \rangle_{0^+_1}$ is the expectation value of $\hat{r}^2$ in the ground state 0^+_1. In the IBM-CM the latter is given by $\langle \hat{r}^2 \rangle = r_c^2 + \alpha N_v + \eta[\langle \hat{n}_d^{(N)} \rangle + \langle \hat{n}_d^{(N+2)} \rangle]$, where r_c^2 is the square radius of the closed shell, N_v is half the number of valence particles, and η is a coefficient that takes into account the effect of deformation [21, 34, 35]. The isotope shift depends on two parameters, $\alpha = 0.235$, $\eta = 0.264$ fm^2, whose values are fixed by the procedure of Ref. [34, 35]. $\Delta \langle \hat{r}^2 \rangle_{0^+_1}$ should increase at the transition point and decrease and, as seen in Figure 6(b), it does so, although the error bars are large and no data are available beyond neutron number 60. (In the large N limit, this quantity, proportional to the derivative of the order parameter $\langle \hat{n}_d \rangle_{0^+_1}$, diverges at the critical point).

Similarly, the two-neutron separation energies S_{2n} can be written as [21], $S_{2n} = -\tilde{A} - \tilde{B} N_v \pm S_{2n}^{\rm def} - \Delta_n$, where $S_{2n}^{\rm def}$ is the contribution of the deformation, obtained by the expectation value of the Hamiltonian in the ground state 0^+_1. The $+$ sign applies to particles and the $-$ sign to holes, and Δ_n takes into account the neutron subshell closure at 56, $\Delta_n = 0$ for 50-56 and $\Delta_n = 2$ MeV for 58-70. The value of Δ_n is taken from Table XII of [36] and $\tilde{A} = -16.5$, $\tilde{B} = 0.758$ MeV are determined by a fit to binding energies of ^{92,94,96}Zr. The calculated S_{2n}, shown in Figure 6(c), displays a complex behavior. Between neutron number 52 and 56 it is a straight line, as the ground state is spherical (seniority-like) configuration (A). After 56, it first goes down due to the subshell closure at 56, then it flattens as expected from a first-order QPT (see, for example the same situation in the $_{62}$Sm isotopes [30]). After 62, it goes down again due to the increasing of deformation and finally it flattens as expected from a crossover from SU(3) to SO(6).

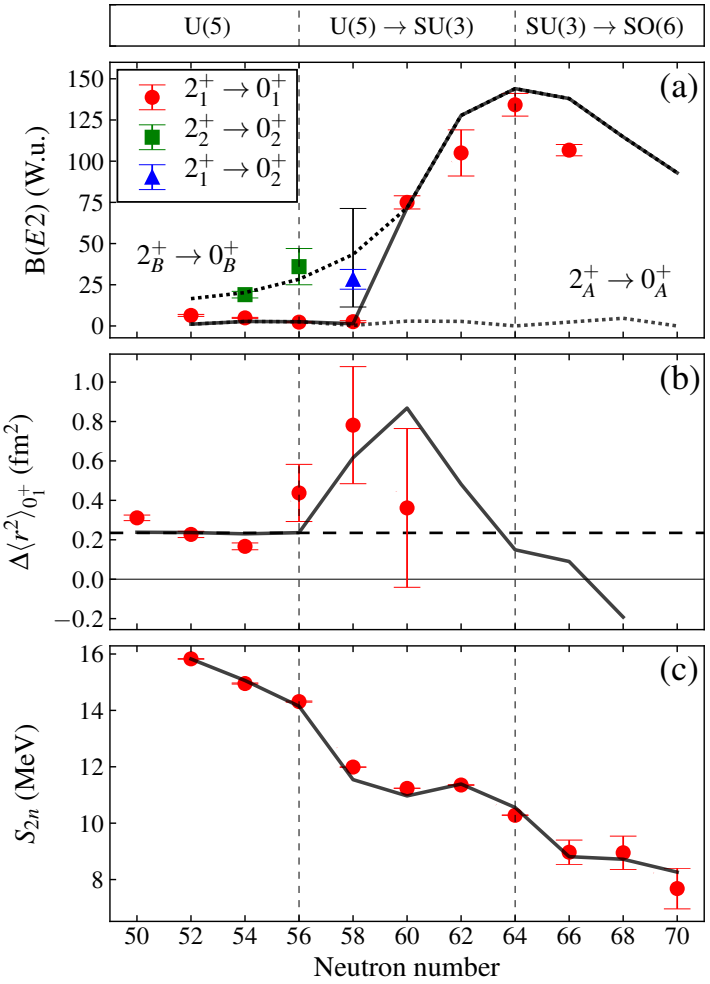

Figure 6. Empirical signatures for QPTs in the Zr chain. Symbols (solid lines) denote experimental data (calculated results). (a) $B(E2)$ values in Weisskopf units (W.u.). Data taken from [9–12, 14, 15, 31]. Dotted lines denote calculated $E2$ transitions within a configuration. (b) Isotope shift, $\Delta\langle\hat{r}^2\rangle_{0_1^+}$ in fm^2. Data taken from [32]. The horizontal dashed line at 0.235 fm^2 represents the smooth behavior in $\Delta\langle\hat{r}^2\rangle_{0_1^+}$ due to the $A^{1/3}$ increase of the nuclear radius. (c) Two-neutron separation energies, S_{2n}, in MeV. Data taken from AME2016 [33]. Adapted from [8].

6 Quantum and Classical Analyses

One of the main advantages of the algebraic method is that one can do both a quantum and a classical analysis. The calculations describe the experimental data in the entire range $^{92-110}$Zr very well. A full account is given in [37]. Here we show only three examples, ^{98}Zr, ^{100}Zr and ^{102}Zr.

^{98}Zr, in Figures 7(a) and 7(b), has a spherical [U(5)-like] ground state configuration (A) and a weakly-deformed [U(5)-perturbed] excited configuration (B). ^{100}Zr, in Figures 7(c) and 7(d), is near the critical point of both Type I and Type II QPTs. The ground state band, has now become configuration (B), and appears to have features of the so-called X(5) symmetry [38], while the spherical configuration (A) has now become the excited band 0^+_2. ^{102}Zr, in Figures 7(e) and 7(f), exhibits well developed deformed [SU(3)-like] rotational bands assigned to configuration (B). States of configuration (A) have shifted to higher energies.

A geometric visualization of the IBM-CM is obtained by introducing coherent (intrinsic) states [39, 40] and constructing an energy-surface matrix whose entries are the matrix elements of the Hamiltonian (2) between the intrinsic states

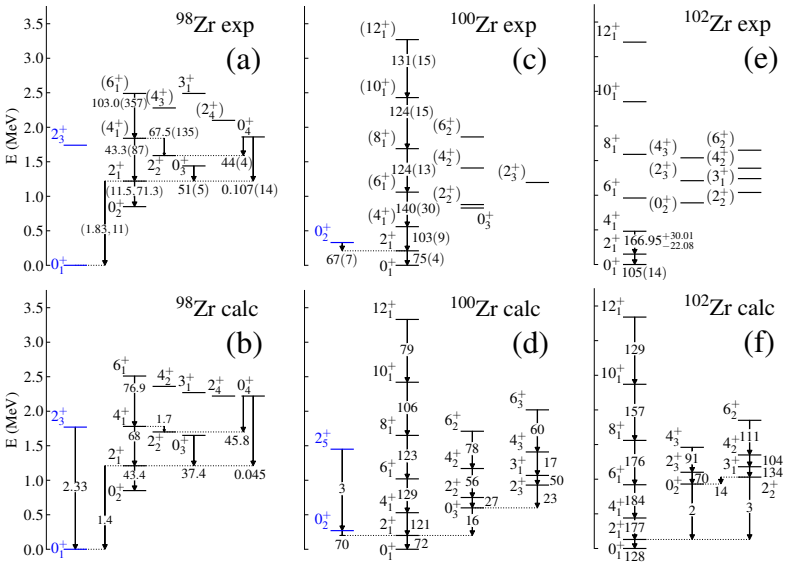

Figure 7. Experimental [12, 14, 15, 31] (top row) and calculated (bottom row) energy levels in MeV and $E2$ rates in W.u. for ^{98}Zr [panels (a)-(b)], ^{100}Zr [panels (c)-(d)] and ^{102}Zr [panels (e)-(f)]. The levels (0^+_1, 2^+_3) in ^{98}Zr and (0^+_2, 2^+_5) in^{100}Zr are dominated by the normal (A) configuration. All other levels shown are dominated by the intruder (B) configuration. Assignments are based on the decomposition of Eq. (4). Panels (c)-(d) are adapted from [8].

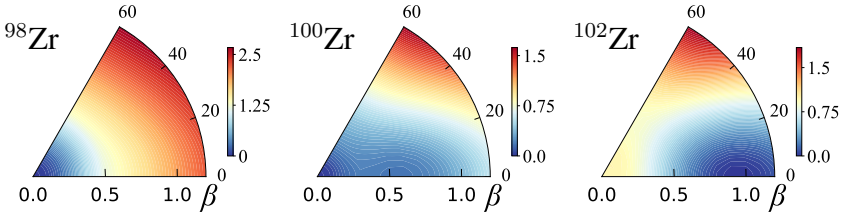

Figure 8. Contour plots in the (β, γ) plane of the lowest eigen-potential surface, $E_-(\beta, \gamma)$, for ^{98}Zr, ^{100}Zr and ^{102}Zr. Adapted from [8].

of the two configurations. Diagonalization of this two-by-two matrix produces the so-called eigen-potentials, $E_\pm(\beta, \gamma)$ [7]. In Figure 8, we show the calculated lowest eigen-potential $E_-(\beta, \gamma)$ for the isotopes described in Figure 7. In general, these classical potentials confirm the quantum results, as they show a transition from spherical ($^{92-98}$Zr), to a flat-bottomed potential at ^{100}Zr, to prolate axially-deformed ($^{102-104}$Zr), and finally to γ-unstable ($^{106-110}$Zr).

In general, the results of the current phenomenological study resemble those obtained in the microscopic approach of the MCSM [19] (which focuses on spectra and $E2$ rates), however, there are some noticeable differences. Specifically, the replacement γ-unstable $\rightarrow$ triaxial and the inclusion of more than two configurations in the MCSM. The spherical state in ^{100}Zr is identified in the MCSM as 0^+_4, in contrast to 0^+_2 in the current calculation and the data. Both calculations show a large jump in $B(E2; 2^+_1 \rightarrow 0^+_1)$, between ^{98}Zr and ^{100}Zr, typical of a first-order QPT. This is in contrast with mean-field based calculations [16–18], which due to their character smooth out the phase transitional behavior, and show no such jump at the critical point of the QPT (see Figure 2 of [15]). The observed peak in $B(E2; 2^+_1 \rightarrow 0^+_1)$ for ^{104}Zr, is reproduced by the current calculation but not by the MCSM.

Acknowledgements

This work was supported in part by the US-Israel Binational Science Foundation Grant No. 2016032 and by the U.S. DOE under Grant No. DE-FG02-91ER-40608. We thank R. F. Casten and J. E. García-Ramos for insightful discussions.

References

[1] R. Gilmore, D.H. Feng (1978) *Phys. Lett. B* **76** 26.
[2] R. Gilmore (1979) *J. Math. Phys.* **20** 891.
[3] P. Cejnar J. Jolie (2009) *Prog. Part. Nucl. Phys.* **62** 210.
[4] P. Cejnar, J. Jolie, R.F. Casten (2010) *Rev. Mod. Phys.* **82** 2155.

[5] F. Iachello (2011) *Rivista del Nuovo Cimento* **34** 617.
[6] K. Heyde, J.L. Wood (2011) *Rev. Mod. Phys.* **83** 1467.
[7] A. Frank, P. Van Isacker, F. Iachello (2006) *Phys. Rev. C* **73** 061302(R).
[8] N. Gavrielov, A. Leviatan, F. Iachello (2019) *Phys. Rev. C* **99** 064324.
[9] A. Chakraborty *et al.* (2013) *Phys. Rev. Lett.* **110** 022504.
[10] F. Browne *et al.* (2015) *Phys. Lett. B* **750** 448.
[11] C. Kremer *et al.* (2016) *Phys. Rev. Lett.* **117** 172503.
[12] S. Ansari *et al.* (2017) *Phys. Rev. C* **96** 054323.
[13] N. Paul *et al.* (2017) *Phys. Rev. Lett.* **118** 032501.
[14] W. Witt *et al.* (2018) *Phys. Rev. C* **98** 041302(R).
[15] P. Singh *et al.* (2018) *Phys. Rev. Lett.* **121** 192501.
[16] J.-P. Delaroche *et al.* (2010) *Phys. Rev. C* **81** 014303.
[17] H. Mei *et al.* (2012) *Phys. Rev. C* **85** 034321.
[18] K. Nomura *et al.* (2016) *Phys. Rev. C* **94** 044314.
[19] T. Togashi, Y. Tsunoda, T. Otsuka, N. Shimizu (2016) *Phys. Rev. Lett.* **117** 172502.
[20] J.E. García-Ramos, K. Heyde (2019) *Phys. Rev. C* **100** 044315.
[21] F. Iachello, A. Arima (1987) "*The Interacting Boson Model*". Cambridge University Press, Cambridge.
[22] P.D. Duval, B.R. Barrett (1981) *Phys. Lett. B* **100** 223; (1982) *Nucl. Phys. A* **376** 213.
[23] M. Sambataro, G. Molnár (1982) *Nucl. Phys. A* **376** 201.
[24] J.E. García-Ramos, V. Hellemans, K. Heyde (2011) *Phys. Rev. C* **84**, 014331.
[25] J.E. García-Ramos, K. Heyde (2014) *Phys. Rev. C* **89** 014306; (2015) *Phys. Rev. C* **92** 034309.
[26] A. Leviatan, N. Gavrielov, J.E. García-Ramos, P. Van Isacker, *Phys. Rev. C* **98** 031302(R).
[27] P. Federman, S. Pittel (1979) *Phys. Rev. C* **20** 820.
[28] K. Heyde, P. Van Isacker, R.F. Casten, J.L. Wood (1985) *Phys. Lett. B* **155** 303.
[29] K Heyde *et al.* (1987) *Nucl. Phys. A* **466** 189.
[30] O. Scholten, F. Iachello, A. Arima (1978) *Ann. Phys.* **115** 325.
[31] Evaluated Nuclear Structure Data File (ENSDF), https://www.nndc.bnl.gov/ensdf/.
[32] I. Angeli, K.P. Marinova (2013) *At. Data Nucl. Data Tables* **99** 69.
[33] M. Wang *et al.* (2017) *Chinese Phys. C* **41** 030003.
[34] S. Zerguine, P. Van Isacker, A. Bouldjedri, S. Heinze (2008) *Phys. Rev. Lett.* **101** 022502.
[35] S. Zerguine, P. Van Isacker, A. Bouldjedri (2012) *Phys. Rev. C* **85** 034331.
[36] J. Barea, F. Iachello (2009) *Phys. Rev. C* **79** 044301.
[37] N. Gavrielov, Ph.D. Thesis, The Hebrew University, Jerusalem, Israel.
[38] F. Iachello (2001) *Phys. Rev. Lett.* **87** 052502.
[39] J.N. Ginocchio, M. W. Kirson (1980) *Phys. Rev. Lett.* **44** 1744.
[40] A.E.L. Dieperink, O. Scholten, F. Iachello (1980) *Phys. Rev. Lett.* **44** 1747.